



## Differential formulation and numerical solution for elastic arches with variable curvature and tapered cross-sections

J. Melchiorre <sup>a</sup>, A. Manuello <sup>a,\*</sup>, F. Marmo <sup>b</sup>, S. Adriaenssens <sup>c</sup>, G.C. Marano <sup>a</sup>

<sup>a</sup> Department of Structural Building and Geotechnics, Politecnico di Torino, Corso Duca degli Abruzzi, 24 10129, Torino, Italy

<sup>b</sup> Department of Structures for Engineering and Architecture, Università degli Studi di Napoli Federico II, Corso Umberto I, 40 80138, Napoli, Italy

<sup>c</sup> Department of Civil and Environmental Engineering E208 Engineering Quadrangle Princeton, NJ 08544, USA

### ARTICLE INFO

#### Keywords:

Ordinary differential equation  
Finite difference method  
Arch  
Curved beam  
Equilibrium  
Volume minimization

### ABSTRACT

In this paper, an alternative analytical and numerical formulation is presented for the solution of a system of static and kinematic ordinary differential equations for curved beams. The formulation is represented here as being useful in the structural evaluation of arch structures and it is propaedeutic to be used in optimization frameworks. Using a finite-difference method, this approach enables the evaluation of the best solution sets accounting for (1) various arch shapes (i.e. circular, quadratic and quartic polynomial forms); (2) different loading combinations; (3) cross-sections varying along the arch span; and (4) different global radius of arch curvature. The presented original approach based on finite-difference, produces solutions with a good precision in a reasonable computational time. This method is applied to 4 different arch case studies with varying rise, cross-section, loading and boundary conditions. Results show good agreement with those obtained using a numerical finite element approach. The presented approach is useful for the (preliminary) design of arches, a common and efficient structural typology for road and railway bridges and large span roofs. As far as buckling verifications are concerned, the comparisons in terms of maximum acting axial force and critical axial force computed is reported in order to consider the effect of instability phenomena coming to trace for each arch configuration the feasible domain.

### 1. Introduction

Since antiquity arches have been used as efficient load bearing structures. Today long-span arches supporting rail and road decks or roofs are selected by structural designers and architects for their stability, efficiency, high loading capacity and their architectural and urban form-making potentialities according to variable curvature and stiffness (Jasińska and Kropiowska, 2018). One of the first key-concept for arch structures is represented by the fact that efficiency of the arch structure is strongly related to its shape: it is difficult to find another type of structure where the connection between geometry and internal loading is so pronounced. The selection of the best arch geometry is key in reducing the structural volume (Marano et al., 2014; Allen and Zalewski, 2009; Wang and Wang, 2015; Bertetto and Marano, 2022; Melchiorre et al., 2021) because effective arch shape allows for the predominance of axial internal actions with low or no eccentricity under a wide range of loading combinations. For a thorough literature review on the history of the study of arches, the reader is referred to Heyman and Jacques (1998) and Kurrer (2008). In particular, a wide range of

analytical studies has been published on the topic of elastic arch bridge, masonry structures and elastic restrained arches (Bresse, 1854; Winkler, 1858; McCullough and Thayer, 1931; Heyman, 1969; Ochsendorf, 2006; Alexakis and Makris, 2015; Pi et al., 2007; Aita et al., 2015; Hu et al., 2018). It can be noted that, many researchers have focused on the behavior of masonry arches while other employed linear analysis of elastic arches to find arch geometries without moments (Lewis, 2016) and closed-form solutions to funicular arches (Wang and Wang, 2015). Other studies accounted for the effects related to geometric and material non-linearity on the general and buckling behavior of these kind of structures (Pi et al., 2007; Aita et al., 2015; Hu et al., 2018). As far as the arch shape is concerned, a recent work presented closed-form formulations for the analysis of the reactions of segmental, catenary and parabolic arches and internal forces of symmetric linear elastic segmental arches subjected to self-weight (Glisic, 2019). It was also shown that under self-weight and a uniformly distributed load, the catenary arch shape with a constant cross-section exhibits lower

\* Corresponding author.

E-mail address: [amedeo.manuellobertetto@polito.it](mailto:amedeo.manuellobertetto@polito.it) (A. Manuello).

internal stresses in comparison with a parabolic arch (Manuello, 2020). Other studies have looked at the optimal shape of isostatic arches under uniform vertical loads (Trentadue et al., 2018; Farshad, 1976; Kimura et al., 2020) or those subjected to a range of loading and constraint conditions (Farshad, 1976; Hu et al., 2010; Osserman, 2010; Michiels and Adriaenssens, 2018; Halpern and Adriaenssens, 2015a; Marmo, 2021). At the same time, other recent works focus on arch form finding (Michiels and Adriaenssens, 2018) and shape optimization (Eliáš et al., 2013; Habbal, 1998; Pouraminian and Ghaemian, 2015; Kumarci et al., 2009; Park et al., 2016; Halpern and Adriaenssens, 2015b; Bruno et al., 2016). Besides addressing the arch geometry, the variation (or even optimization) of the cross-section along the arch is another avenue to further achieve design efficiency (Marano et al., 2014; Szefer and Mikulski, 1984).

Numerical analysis of arches can be performed by using the finite element method. An approximate way to account for the curved geometry is that of employing a series of linear beam elements that approximate the arch's curved geometry by linear segments. Such a modeling approach implies that the transverse loads are in equilibrium with shear variations only (Carpinteri, 2013). Conversely, for curved beams, both shear and axial forces contribute to balance the applied loads. As a result, the employment of straight beam elements may produce significant inaccuracies in the determination of internal forces. In arches, this produces a visible oscillation of the shear force about the actual solution. One of the possible solutions to the problem could involve increasing the number of finite elements that constitute the model. More accurate solutions can be obtained by employing curved beam finite elements (Tufekci et al., 2017; Litewka and Rakowski, 1997; Benedetti and Tralli, 1989; Ibrahimbegović, 1995; Nascimbene, 2013). Alternative approaches rely on the isogeometric analysis (Bauer et al., 2016), where both the beam shape and the displacement field are described by NURBS functions.

In this paper, starting from the set of differential equations holding for plane linear elastic curved beams, a unique sixth order differential equation is derived by employing simplifying assumptions. This equation, together with the relevant boundary conditions, is used to evaluate displacements, internal forces and Cauchy stresses for elastic arches having variable curvature and tapered cross-section. The proposed lean approach is then validated by comparison with finite element solutions and is used to perform a series of parametric analyses useful to derive, in an efficient, preliminary way, practical indications for the conceptual design of elastic arches.

Recently, many researchers have developed similar models for the study of the arches, for example Sonavane (2014) applied basic principles of the flexibility method in the analysis and design of symmetrical circular arches under different loading conditions. El Zareef et al. (2019) studied an analytical model of curved elements with constant cross-section. In this paper, the sixth order differential equation is retrieved with the aim of maintaining the solution as general as possible. This means that it can be applied to a wide range of arch structures with different shapes and variable cross-sections.

The presented method is propaedeutic to be used in optimization frameworks and for this reason, the analytical-numerical formulation in this paper can be a good alternative to the more popular Finite Element Method (FEM) or Isogeometric Analysis (IGA), since the proposed method performs the calculation with as less computational effort. For this reason the problem is solved using the Finite Difference Method (FDM) that, differently from the FEM and the IGA, does not require the definition of shape functions. In the presented case, this shape function would be of a degree higher than 5, with a consequently high computational effort. Using the FDM, instead, produces results of higher accuracy as the number of nodes is increased without specific computational limitations. The FDM is frequently used for the solution of structural engineering problems, for example Jirásek et al. (2021) proposed a FDM-based method for the calculation of a two-dimensional geometrically non-linear beam element, or Shi et al. (2020) that studied

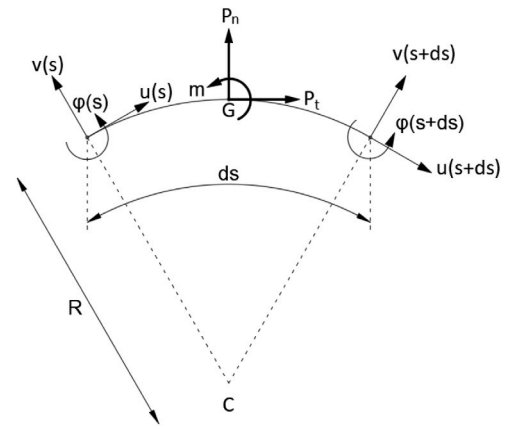


Fig. 1. Displacements induced by external forces on an infinitesimal beam segment.

the bridge-embankment transition by combining the discrete element method (DEM) with the FDM, or Li et al. (2017) with their response sensitivity analysis for plastic plane problems based on direct differentiation method in which the FDM is used as a reference to validate their results.

The proposed method is based on an analytical-numerical approach. Many researchers have developed similar models for the study of the arches, for example Sonavane (2014) applied basic principles of the flexibility method in the analysis and design of symmetrical circular arches under different loading conditions. El Zareef et al. (2019) studied an analytical model of curved elements with constant cross-section. In this paper, the sixth order differential equation is retrieved with the aim of maintaining the solution as general as possible. This means that it can be applied to a wide range of arch structures with different shapes and variable cross-sections.

The paper is organized as follows. In Section 2 the basic sixth-order differential equation that describes the mechanics of the arch is derived from the general equations holding for planar curved beams. Sections 2.1 and 2.2 address the boundary conditions and the computation of displacements and internal forces along the arch axis. In Section 3 it is described how the variability of the radius of curvature, of the cross section inertia and different loading conditions are implemented within the numerical solving procedure based on the finite difference method. Moreover, in Section 4 a set of numerical examples that validate the new approach are presented. This set shows the approach's versatility to perform parametric studies on arches. Finally, as far as buckling verifications are concerned, in the paper the comparisons in terms of maximum acting axial force and critical axial force computed by a simplified method is reported in order to consider the effect of instability phenomena coming to trace for each arch configuration the feasible domain.

## 2. Formulation of the problem

The mechanical behavior of arches can be described by employing the model of curved beams. A plane beam having a curved axis and variable cross section of inertia  $J(s)$ ,  $s$  being the curvilinear coordinate defined along the beam axis, is considered. The beam is composed of homogeneous linear elastic material having Young modulus  $E$ . The radius of curvature of the beam axis is represented by the function  $R(s)$ , e.g., see Fig. 1.

The strain-displacement relations are (Carpinteri, 2013):

$$\epsilon = u^{(1)} + \frac{v}{R} \quad \gamma = v^{(1)} - \frac{u}{R} + \varphi \quad \chi = \varphi^{(1)} \quad (1)$$

where  $\epsilon$ ,  $\gamma$  and  $\chi$  are the normal strain, shear strain and elastic curvature of the beam, while  $\varphi$ ,  $u$  and  $v$  are the rotation and the

tangential and normal displacements of the generic beam cross section, respectively. These quantities are a function of the curvilinear abscissa  $s$ . However this dependence is omitted to simplify notation. Lagrange's notation is used for derivatives, hence  $u^{(d)}$  is the  $d$ th order derivative of the function  $u$  with respect to the curvilinear abscissa  $s$ .

Neglecting the beam elongation, i.e. setting  $\epsilon = 0$ , the first formula of (1) gives

$$v = -Ru^{(1)} \tag{2}$$

Similarly, neglecting the shear strain, i.e. setting  $\gamma = 0$ , from the second formula of (1) one has

$$\varphi = -Ru^{(2)} - R^{(1)}u^{(1)} - \frac{1}{R}u \tag{3}$$

where Eq. (2) has been used to write  $v^{(1)} = -Ru^{(2)} - R^{(1)}u^{(1)}$ .

The Eqs. (1), (2) and (3) are used to describe the beam deformation by the elastic curvature  $\chi$  only, that is

$$\chi = -Ru^{(3)} - 2R^{(1)}u^{(2)} - \left[ R^{(2)} + \frac{1}{R} \right] u^{(1)} + \frac{R^{(1)}}{R^2}u \tag{4}$$

Equilibrium equations of the beam are (Carpinteri, 2013):

$$N^{(1)} + \frac{V}{R} + P_t = 0 \quad V^{(1)} - \frac{N}{R} + P_n = 0 \quad M^{(1)} + V + m = 0 \tag{5}$$

where  $N$ ,  $V$  and  $M$  are the axial force, shear force and bending moment.  $P_t$  and  $P_n$  are the external loads applied along the tangential and normal direction, while  $m$  is the distributed moment.

From the third equation in (5) one has

$$V = -M^{(1)} - m \tag{6}$$

Substitution this expression of  $V$  into (5)<sub>2</sub> gives

$$N = R(P_n - M^{(2)} - m^{(1)}) \tag{7}$$

Employing (6) and (7) into (5) yields

$$RM^{(3)} + R^{(1)}M^{(2)} + \frac{1}{R}M^{(1)} = P_t + R^{(1)}P_n + RP_n^{(1)} - \frac{m}{R} - R^{(1)}m^{(1)} - Rm^{(2)} \tag{8}$$

The bending moment  $M$  can be expressed as a function of the elastic curvature  $\chi$  by employing the beam constitutive equation

$$M = EJ\chi \tag{9}$$

where  $EJ$  is the bending stiffness of the beam cross section. The derivatives of  $M$  appearing in Eq. (8) are determined by differentiating the constitutive equation as

$$M^{(1)} = E(J^{(1)}\chi + J\chi^{(1)}) \tag{10}$$

$$M^{(2)} = E(J^{(2)}\chi + 2J^{(1)}\chi^{(1)} + J\chi^{(2)}) \tag{11}$$

$$M^{(3)} = E(J^{(3)}\chi + 3J^{(2)}\chi^{(1)} + 3J^{(1)}\chi^{(2)} + J\chi^{(3)}) \tag{12}$$

where both  $R$  and  $J$  are assumed to be a function of  $s$ , while  $E$  is assumed to be constant.

The expression of  $\chi$  and its derivatives can be obtained from (4) and can be expressed as a combination of the  $R$  and  $u$  and their derivatives. Factoring out the derivatives of  $u$ , the generic expression of the  $d$ th order derivative of  $\chi$ ,  $d = 0, \dots, 3$ , is

$$\chi^{(d)} = a_d u^{(6)} + b_d u^{(5)} + c_d u^{(4)} + d_d u^{(3)} + e_d u^{(2)} + f_d u^{(1)} + g_d u \tag{13}$$

where  $\chi^{(0)} = \chi$  is the 0-th order derivative of  $\chi$ . Functions  $a_d, \dots, g_d$  are expressed in terms of  $R$  and its derivatives; their expressions are given in Table 1.

Employing Eqs. (10)–(13) into (8) a sixth order differential equation in terms of  $u$  is obtained. It reads

$$au^{(6)} + bu^{(5)} + cu^{(4)} + du^{(3)} + eu^{(2)} + fu^{(1)} + gu + h = 0 \tag{14}$$

where the functions  $a, \dots, g$  are expressed in terms of the functions defined in Table 1,  $R$ ,  $J$  and their derivatives. In particular, indicating

by  $C$  the generic function of the set  $\{a, \dots, g\}$  and by  $C_d$ ,  $d = 0, \dots, 3$ , the corresponding functions in Table 1, the generic expression for  $a, \dots, g$  is

$$C = \left( RJ^{(3)} + R^{(1)}J^{(2)} + \frac{1}{R}J^{(1)} \right) C_0 + \left( 3RJ^{(2)} + 2R^{(1)}J^{(1)} + \frac{1}{R}J \right) C_1 + \left( 3RJ^{(1)} + R^{(1)}J^{(1)} \right) C_2 + RJ C_3 \tag{15}$$

Finally, the function  $h$  used in Eq. (14) is

$$h = \frac{1}{E} \left( P_t + R^{(1)}P_n + RP_n^{(1)} - \frac{m}{R} - R^{(1)}m^{(1)} - Rm^{(2)} \right) \tag{16}$$

### 2.1. Boundary conditions

Eq. (14) describes the behavior of a planar curved beam having a cross section whose inertia  $J$  is functionally variable along the beam axis. It has been obtained by neglecting axial and shear deformations, i.e. it is set  $\epsilon = 0$  and  $\gamma = 0$ , hence this model accounts for bending deformation only. These assumptions have been used to obtain a differential equation that is expressed uniquely as a function of the tangential displacement  $u$ . In order to solve this equation, proper boundary conditions need to be considered and expressed as a function of the values of  $u$  and/or its derivatives at the two extremities of the beam. These conditions are used to model restraints at the arch springers, that either correspond to a full restrain or a hinge (Fig. 2).

For a fully restrained arch it is set

$$\begin{aligned} u(0) &= u(L_{arch}) = 0 \\ v(0) &= v(L_{arch}) = 0 \\ \varphi(0) &= \varphi(L_{arch}) = 0 \end{aligned} \tag{17}$$

Using Eqs. (2) and (3), the boundary conditions (17)<sub>2</sub> and (17)<sub>3</sub> are rewritten as a function of the values of  $u^{(1)}$  and  $u^{(2)}$  as

$$\begin{aligned} u^{(1)}(0) &= u^{(1)}(L_{arch}) = 0 \\ u^{(2)}(0) &= u^{(2)}(L_{arch}) = 0 \end{aligned} \tag{18}$$

For a hinged arch, boundary conditions are

$$\begin{aligned} u(0) &= u(L_{arch}) = 0 \\ v(0) &= v(L_{arch}) = 0 \\ M(0) &= M(L_{arch}) = 0 \end{aligned} \tag{19}$$

Likewise the case of a fully restrained arch, the boundary conditions (19)<sub>2</sub> is rewritten as (19)<sub>1</sub>. Furthermore, combining (4) and (9), the conditions (19)<sub>3</sub> are rewritten as

$$\begin{aligned} R(0)u^{(3)}(0) + 2R^{(1)}(0)u^{(2)}(0) &= 0 \\ R(L_{arch})u^{(3)}(L_{arch}) + 2R^{(1)}(L_{arch})u^{(2)}(L_{arch}) &= 0 \end{aligned} \tag{20}$$

### 2.2. Evaluation of displacements and internal forces

The solution of the differential Eq. (14) and the boundary conditions described in Section 2.1 allow to compute the values of  $u$  along the entire length of the arch. The numerical solution strategy is addressed in next section. However, once  $u$  is determined, the remaining displacement components and the internal forces can be retrieved. Actually, formula (2) is used to evaluate the radial displacement and (3) to determine the cross-section rotation.

The elastic curvature  $\chi$  is also computed from  $u$  by employing formula (4). It is used to compute the bending moment from formula (9). Also the shear and the axial force can be computed as a function of  $\chi$  by employing (9), (6) and (7), obtaining

$$V = E(J^{(1)}\chi + J\chi^{(1)}) + m \tag{21}$$

$$N = R \left[ P_n - E(J^{(2)}\chi + 2J^{(1)}\chi^{(1)} + J\chi^{(2)}) - m^{(1)} \right] \tag{22}$$

**Table 1**  
Functions used to express  $\chi$  and its derivatives by Eq. (13).

$a_0 = 0$	$b_0 = 0$
$a_1 = 0$	$b_1 = 0$
$a_2 = 0$	$b_2 = R$
$a_3 = R$	$b_3 = 5R^{(1)}$
$c_0 = 0$	$d_0 = R$
$c_1 = R$	$d_1 = 3R^{(1)}$
$c_2 = 4R^{(1)}$	$d_2 = 6R^{(2)} + \frac{1}{R}$
$c_3 = 10R^{(2)} + \frac{1}{R}$	$d_3 = 10R^{(3)} - 4R^{(1)}\frac{1}{R^2}$
$e_0 = 2R^{(1)}$	$f_0 = R^{(2)} + \frac{1}{R}$
$e_1 = 3R^{(2)} + \frac{1}{R}$	$f_1 = R^{(3)} - 2R^{(1)}\frac{1}{R^2}$
$e_2 = 4R^{(3)} - 3R^{(1)}\frac{1}{R^2}$	$f_2 = R^{(4)} - 3R^{(2)}\frac{1}{R^2} + 6(R^{(1)})^2\frac{1}{R^3}$
$e_3 = 5R^{(4)} - 6R^{(2)}\frac{1}{R^2} + 12(R^{(1)})^2\frac{1}{R^3}$	$f_3 = R^{(5)} - 4R^{(3)}\frac{1}{R^2} + 24R^{(1)}R^{(2)}\frac{1}{R^3} - 24(R^{(1)})^3\frac{1}{R^4}$
$g_0 = -R^{(1)}\frac{1}{R^2}$	
$g_2 = -R^{(2)}\frac{1}{R^2} + 2(R^{(1)})^2\frac{1}{R^3}$	
$g_2 = -R^{(3)}\frac{1}{R^2} + 6R^{(1)}R^{(2)}\frac{1}{R^3} - 6(R^{(1)})^3\frac{1}{R^4}$	
$g_3 = -R^{(4)}\frac{1}{R^2} + 8R^{(1)}R^{(3)}\frac{1}{R^3} + 6(R^{(2)})^2\frac{1}{R^3} - 36(R^{(1)})^2R^{(2)}\frac{1}{R^4} + 24(R^{(1)})^4\frac{1}{R^5}$	

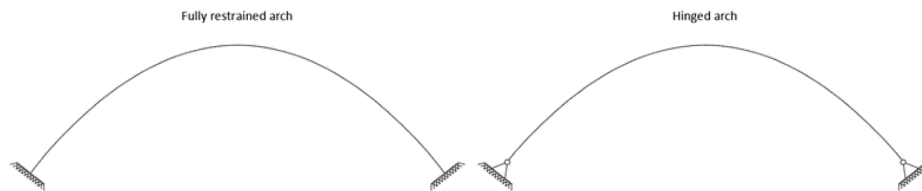


Fig. 2. Boundary conditions.

### 3. Numerical implementation of the solving procedure

The ordinary differential Eq. (14) and the boundary conditions described in Section 2.1 represent a typical sixth order boundary problem. This system of equations can be effectively solved by employing a standard implementation of the finite difference method (FDM).

The motivation for using FDM to the studied problem is the high degree (6th) of the differential Eq. (14) that, in addition, has non-constant coefficients due to the variability of the radius of curvature and of the cross section inertia. If solved by the FEM or IGA, the differential equation needs to be rewritten in weak form and will contain the 3rd derivative of the unknown function,  $u$ . This means that the shape functions (of either the FEM or IGA discretization) are required to be at least of class  $C^3$  (3 times differentiable with continuous derivatives). This is an ultimate condition to make the method well stated and corresponds to constant elastic curvature over each element, which will produce very inaccurate results. Even in the simplest case of constant radius of curvature, constant cross section and null distributed loads, the curvature will be a 2nd order polynomial since it is computed as the 3rd derivative of the tangential displacement  $u$ , see, e.g. Eq. (4),

which, in turn, is the solution of a 6th order homogeneous differential equation, i.e. Eq. (14), and will be of degree 5. Hence, to formulate an acceptably accurate FEM or IGA formulation, applicable to beams of variable curvature and inertia, shape functions are required to be of higher degree with substantial higher computational effort. On the other hand, FDM does not require the definition of any shape function and produces results of higher accuracy as the number of nodes is increased without specific computational limitations.

As usual, the FDM employs the discrete versions of the differential equation and boundary conditions, in which derivatives are computed as a function of the values that each considered quantity attains at a series of  $N$  nodes positioned along the arch axis. Hence, in order to properly employ this method, the functions that describe the radius of curvature of the arch, namely  $R(s)$ , and the inertia of the cross section, that is  $J(s)$ , and the tangential and radial loads,  $P_t$  and  $P_r$ , are considered as given. Since these functions are employed within the FDM, their values need to be computed at the nodes of the discretized arch axis and, if needed, their derivatives are determined numerically by means of usual formulas pertaining to the FDM.

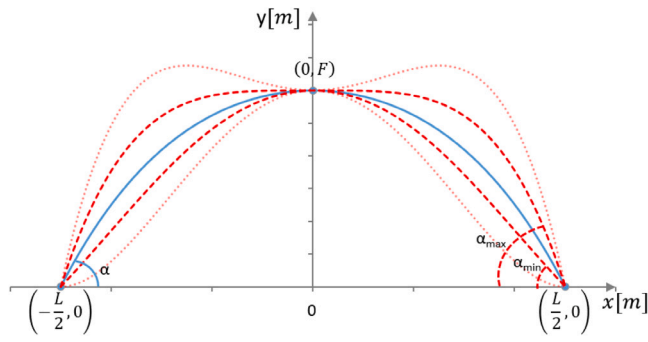


Fig. 3. Limit values for the angles  $\alpha = \arctan(S)$  at the arch springers.

In this section, a procedure is described for assigning the radius of curvature  $R(s)$ , the cross-section inertia  $J(s)$  and the loading functions  $P_t$  and  $P_l$ .

### 3.1. Radius of curvature

Although the solution approach presented in this paper is applicable to arches of arbitrary geometry, hereafter the cases of circular and polynomial arches are considered for brevity. These geometries are defined in a global reference system of axes  $x$  (horizontal) and  $y$  (vertical).

The axis of a circular arch can be defined by the equation of a circumference through three points. In particular, given the arch span  $L$  and rise  $F$ , the arch axis is given as:

$$y_{circ}(x) = \sqrt{\frac{L^2}{4} - x^2} + \frac{1}{4} \left( \frac{L^2}{4F} - F \right) - \frac{1}{2} \left( \frac{L^2}{4F} - F \right) \quad (23)$$

If, instead, the axis of the arch is parabolic, its geometry is simply given as:

$$y_{par}(x) = -\frac{4F}{L^2} x^2 + F \quad (24)$$

that represent the specific instance of a polynomial arch. A generic  $n$ th order polynomial arch has an axis described by the function:

$$y_{n-pol}(x) = p_n x^n + p_{n-1} x^{n-1} + \dots + p_1 x + p_0 \quad (25)$$

where  $p_i, i = 0, \dots, n$  are the real coefficients of the polynomial. Their values are assigned in such a way that the polynomial curve that defines the arch axis fulfills some geometric conditions.

These geometric conditions are used to control the actual shape of the arch. For example, for a fourth order polynomial arch ( $n = 4$ ), the five parameters  $p_0, \dots, p_4$  need to be defined. Symmetry of the arch implies  $p_1 = p_3 = 0$ , while the remaining coefficients are determined by setting the arch span  $L$ , the arch rise  $F$  and the slope  $S$  at the left springer of the arch. Notice that because of symmetry, the slope at the right springer is  $-S$ . Accordingly, one has

$$y_{4-pol}(x) = \left( -4 \frac{S}{L^3} + 16 \frac{F}{L^4} \right) x^4 + \left( \frac{S}{L} - \frac{8F}{L^2} \right) x^2 + F \quad (26)$$

However, not all values of  $S$  define a concave shape and two limit values of  $S$  need to be defined in order to obtain a concave arch, see, e.g., Fig. 3. Such limit values, namely  $S_{min}$  and  $S_{max}$ , can be determined by imposing a negative curvature at the springers and at the midspan, that is:

$$\begin{aligned} y_{4-pol}^{(2)}(-L/2) < 0 &\Rightarrow S_{min} = \frac{16F}{5L} \\ y_{4-pol}^{(2)}(0) < 0 &\Rightarrow S_{max} = 8 \frac{F}{L} \end{aligned} \quad (27)$$

The theoretical slope limits determined by formulas (27) need to be narrowed to avoid numerical instabilities. Such an issue is due to very high values of  $R$  at the arch springers or at mid-span when  $S$  is very

close to either one of such limits. Hence, such limits are substituted by  $S_{min} = 3.5F/L$  and  $S_{max} = 5F/L$  in practical applications.

Once the geometry of the arch axis is defined, e.g. by the generic function  $y(x)$ , its radius of curvature can be computed as (Gray et al., 2017):

$$\hat{R}(x) = -\frac{\sqrt{1 + (y^{(1)})^2}}{y^{(1)}} \quad (28)$$

Notice that above formula defines the radius of curvature as a function of  $x$ . Hence the symbol  $\hat{R}$ . It can be rewritten as a function of the arc-length  $s$  by setting  $R(s) = \hat{R}(x(s))$ . To this end, an explicit expression of the function  $x(s)$  is needed. This function is the inverse of the arc-length function  $s(x)$ , defined as

$$s(x) = \int_{-L/2}^x \sqrt{1 + [y^{(1)}]^2} dx \quad (29)$$

for planar curves. However, the analytical expression of  $s(x)$  is difficult to determine and the analytical evaluation of its inverse is unpractical. However, recalling that the boundary problem is solved by the FDM, only the nodal values of  $R$ , and hence of  $x(s)$ , are necessary.

In particular, the arch axis is modeled as a polygon of  $N$  vertices of coordinates  $(x_i, y_i), i = 1, \dots, N$ , see, e.g., Fig. 4. Hence, being  $x_i < x_{i+1}$ , a generic side of the polygon, that is  $(x_{i-1}, y_{i-1}) - (x_i, y_i), i = 2, \dots, N$ , has length

$$\Delta s_i = \sqrt{(x_i - x_{i-1})^2 + (y_i - y_{i-1})^2} = \sqrt{(\Delta x_i)^2 + (\Delta y_i)^2} \quad (30)$$

Accordingly, the arc-length associated to the generic point of abscissa  $x_i$  is numerically approximated by

$$s(x_i) \approx \sum_{j=2}^i \Delta s_j = s_i \quad (31)$$

holding for  $i = 2, \dots, N$ , while  $s(x_1) = 0$ .

The pairs of values  $(x_i, s_i)$  are used to numerically represent the function  $x(s)$ , so that the values attained by  $R(s)$  at the nodes can be computed as

$$R_i = R(s_i) = \hat{R}(x(s_i)) = -\frac{\sqrt{1 + [y^{(1)}(x(s_i))]^2}}{y^{(1)}(x(s_i))} \quad (32)$$

where  $y^{(1)}$  is obtained by differentiating the function that describes the arch axis.

### 3.2. Inertia of the cross section

The function  $J(s)$  expresses the value of the cross sections' moment of inertia along the curvilinear abscissa  $s$ . To this end, it is useful to compute  $J(s)$  as a function of the characteristic size  $r(s)$  of the arch cross section. As shown in Fig. 5(a),  $r(s)$  represents either the length of the side of a square section or the radius of a circular section. In case the section is rectangular,  $r_1(s)$  is the height of the rectangle, while the width is determined by assuming the aspect ratio  $r_2/r_1$  constant along the arch. For hollow sections, thickness is kept constant along the arch.

For the numerical examples reported below,  $r(s)$  attains the values  $r_{base}$  at the springers and  $r_{mid}$  at the crown and is either expressed as a linear or a quadratic function of  $s$ , see, e.g., Fig. 5(b). Hence, indicating by  $\eta = r_{mid}/r_{base}$  the reduction factor, in the first case it is

$$r_{lin}(s) = \frac{2r_{base}(1-\eta)}{L_{arch}} \left| s - \frac{L_{arch}}{2} \right| + \eta r_{base} \quad (33)$$

while in the latter

$$r_{quad}(s) = -\frac{4r_{base}(1-\eta)}{L_{arch}^2} s^2 + \frac{4r_{base}(1-\eta)}{L_{arch}} s + r_{base} \quad (34)$$

where  $L_{arch}$  is the length of the arch. It is computed by using formula (31) with  $i = N$ .

Notice that in case of a linear variation of  $r$  along the arch, the function  $J(s)$  presents a cusp point at the mid-span. This causes numerical instability that can be avoided by approximating  $J(s)$  by means of a 4-th order polynomial interpolation (Fig. 5(c)).

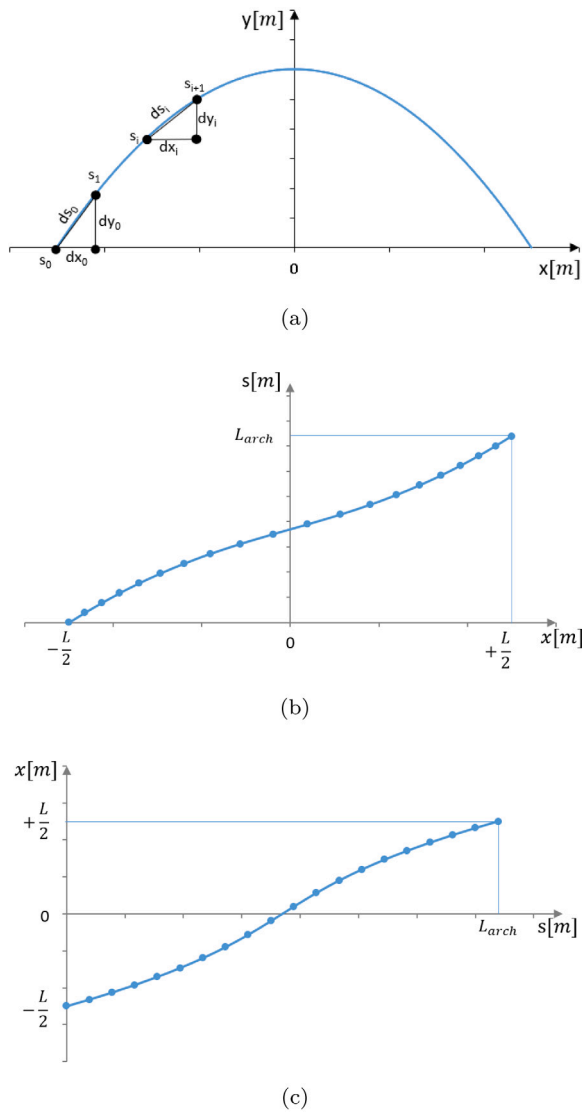


Fig. 4. Discretization of the arch (a), function  $s(x)$  (b) and  $x(s)$  (c).

### 3.3. Loading

Fig. 6 shows some examples of loading configuration that can be applied to the arch axis. External loads are accounted for within the sixth order differential Eq. (14) by the terms  $P_t$  and  $P_n$  in (16). These two functions represent the load applied along the tangential and the normal direction of the curved arch axis and are intended as forces per unit arc-length.

Loads given in the global reference system, i.e. with components  $P_x$  and  $P_y$ , are transformed into the local reference by the transformation formulas

$$\begin{aligned} P_n(s) &= -P_x(s) \sin \alpha(s) + P_y(s) \cos \alpha(s) \\ P_t(s) &= P_x(s) \cos \alpha(s) + P_y(s) \sin \alpha(s) \end{aligned} \quad (35)$$

where  $\alpha(s) = \arctan(y^{(1)}(x))$ . If loads are assigned as forces per unit projected length, i.e. measured along  $x$ , then the loading function needs to be transformed as forces per unit arc-length as

$$P_{(\cdot)}(s_i) = \frac{P_{(\cdot)}(x(s_i))}{\sqrt{1 + [y^{(1)}(x(s_i))]^2}} \quad (36)$$

where it has been used  $x(s_i)$  to represent the node abscissas of the discretized arch axis as it has been done for the radius of curvature.

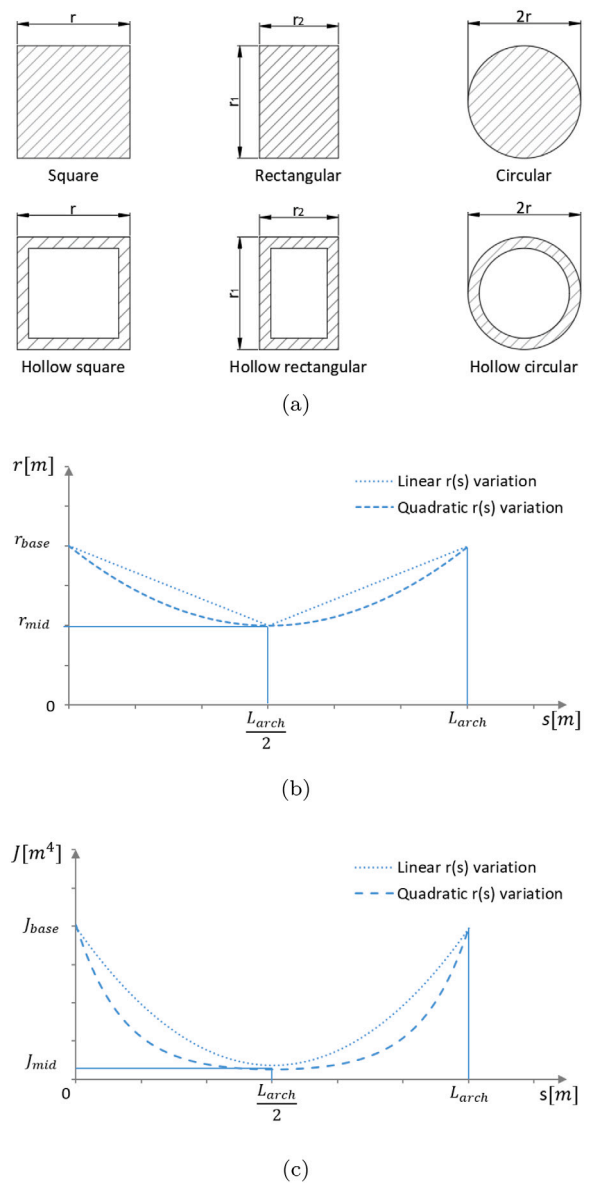


Fig. 5. Definition of the dimension  $r(s)$  on the cross sections (a). Function describing the variation of the characteristic dimension of the section  $r(s)$  (b). Function describing the variation of the inertia  $J(s)$  (c).

## 4. Numerical examples

Described approach has been implemented in MATLAB (2019) where an ad hoc implementation of the finite difference method has been coded. Validation of this implementation has been done by comparing computed results with those obtained from a finite element analysis of the same problems performed in the commercial software MidasGEN (0000). A selected example of such a validation is reported in Section 4.1.

Additional parametric analyses have been performed on selected case studies in order to have design indications for an optimal conceptual design of arches. These analyses are reported in Section 4.2.

### 4.1. Validation

In order to verify the correctness of proposed approach, a series of case studies have been analyzed by varying the axis and cross-section

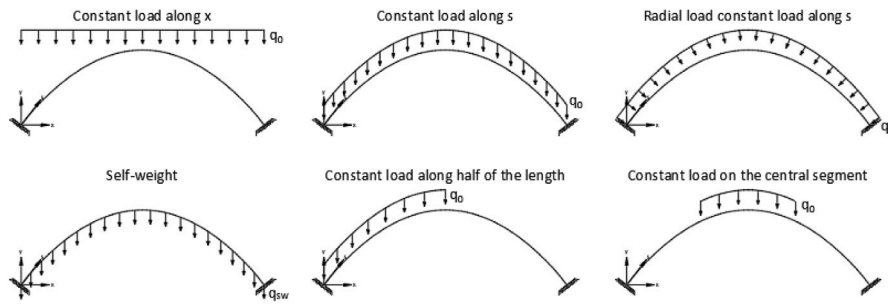
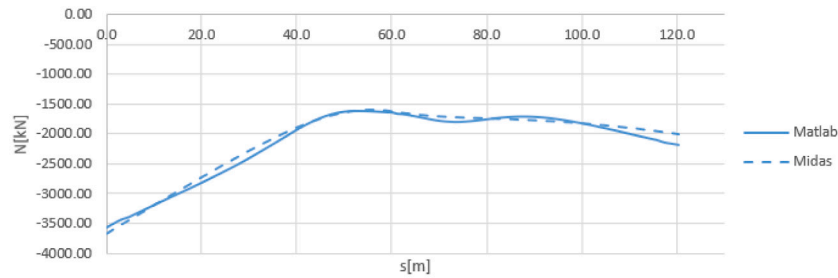
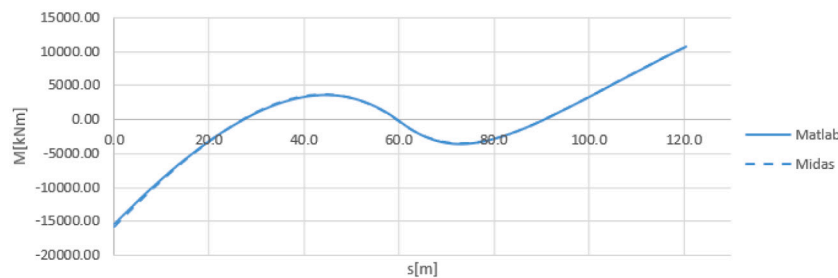


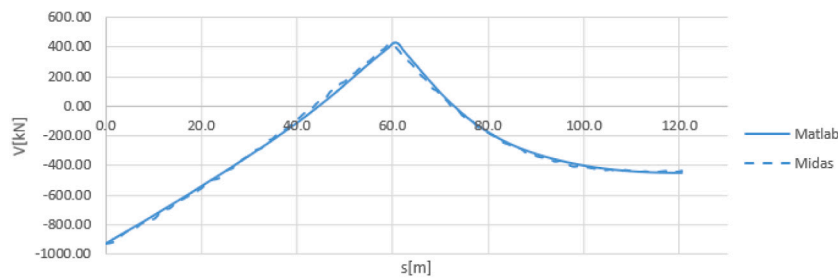
Fig. 6. Some examples of loading configurations.



(a)



(b)



(c)

Fig. 7. Internal actions: Axial force (a), Bending Moment (b), Shear force (c).

geometry, boundary and loading conditions. Among the several analyzed cases, we report hereafter a selected case study made interesting for the variability of the cross section and the non symmetric load case. Also this is the case in which we registered the higher difference between our results and those obtained by the finite element method.

Figs. 7–9 refer to a parabolic arch having span  $L = 100$  m and rise  $F = 30$  m. It is characterized by a hollow circular cross section having radius  $r$  quadratically varying between  $r_{base} = 0.5$  m at the springers and  $r_{mid} = 0.25$  at the crown, while its thickness  $t = 0.1$  m is kept constant along the entire arch. The arch is fully restrained at both extremities

and is subjected to a vertical load  $P_y = -50$  kN/m uniformly distributed along the arch axis and applied to the left half of the arch.

Results are compared in terms of internal forces (Fig. 7), normal stresses (Fig. 8), displacements and rotations with respect to the global coordinate system  $(x, y)$  (Fig. 9). Notice the very good agreement between results obtained from proposed method and those computed from Midas.

It is worth noticing that proposed formulation accounts only for bending deformation of the arch, while axial and shear strain are neglected by the proposed model. In order to verify that axial deformations  $\epsilon$  plays a negligible role in the structural response of elastic

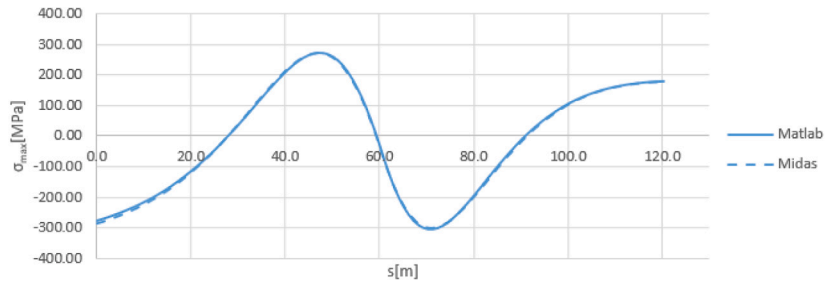
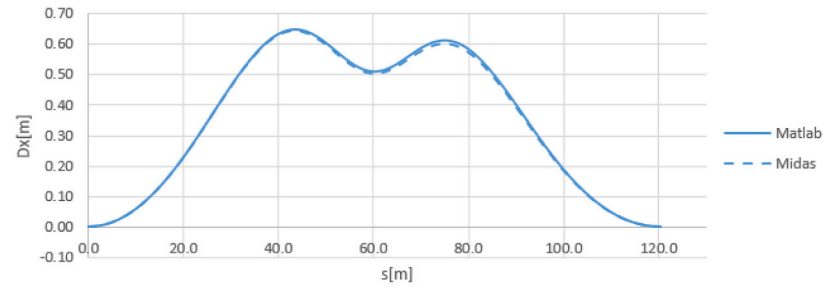
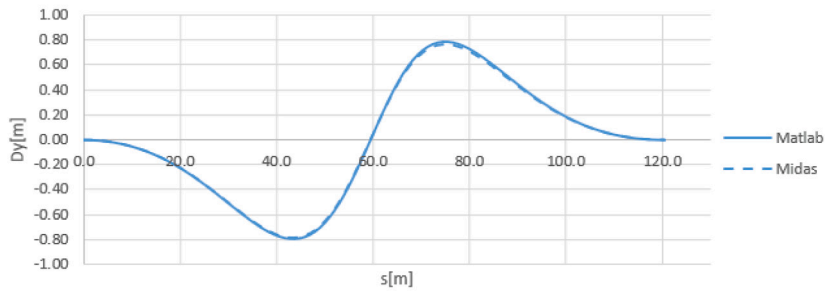


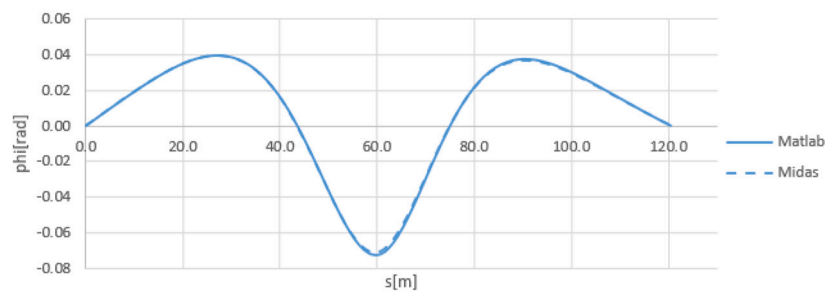
Fig. 8. Normal stresses.



(a)



(b)



(c)

Fig. 9. Displacement in the global coordinate system (x, y): Displacement in the x-direction (a), Displacement in the y direction (b), Rotations (c).

arches, we compare the elastic strain energy relevant to the solutions obtained by both the finite element method and the proposed approach.

The elastic strain energy associated to the finite element solution for considered case study amounts to:

$$E_{el,TOT}^{FEM} = \int_0^{s_{end}} \left( \frac{1}{2} \frac{N^2}{EA} + \frac{1}{2} \frac{M^2}{EJ} \right) ds = 4.51E + 21 \quad (37)$$

and accounts for both the contribution of elongation and bending. Notice that the contribution of shear is, however, neglected since considered finite element results are based on the Euler–Bernoulli beam model.

The elastic strain energy computed for the proposed formulation, instead, accounts for the bending contribution only, that is:

$$E_{el,TOT}^{FDM} = \int_0^{s_{end}} \left( \frac{1}{2} \frac{M^2}{EJ} \right) ds = 4.38E + 21 \quad (38)$$

The obtained values show that, for the considered case study, axial elastic energy is actually negligible: the difference between these two values is below the 3%.

#### 4.2. Parametric analysis of arches

In this section the results of a series of parametric analysis performed on thousands of arches having different shapes, cross section,

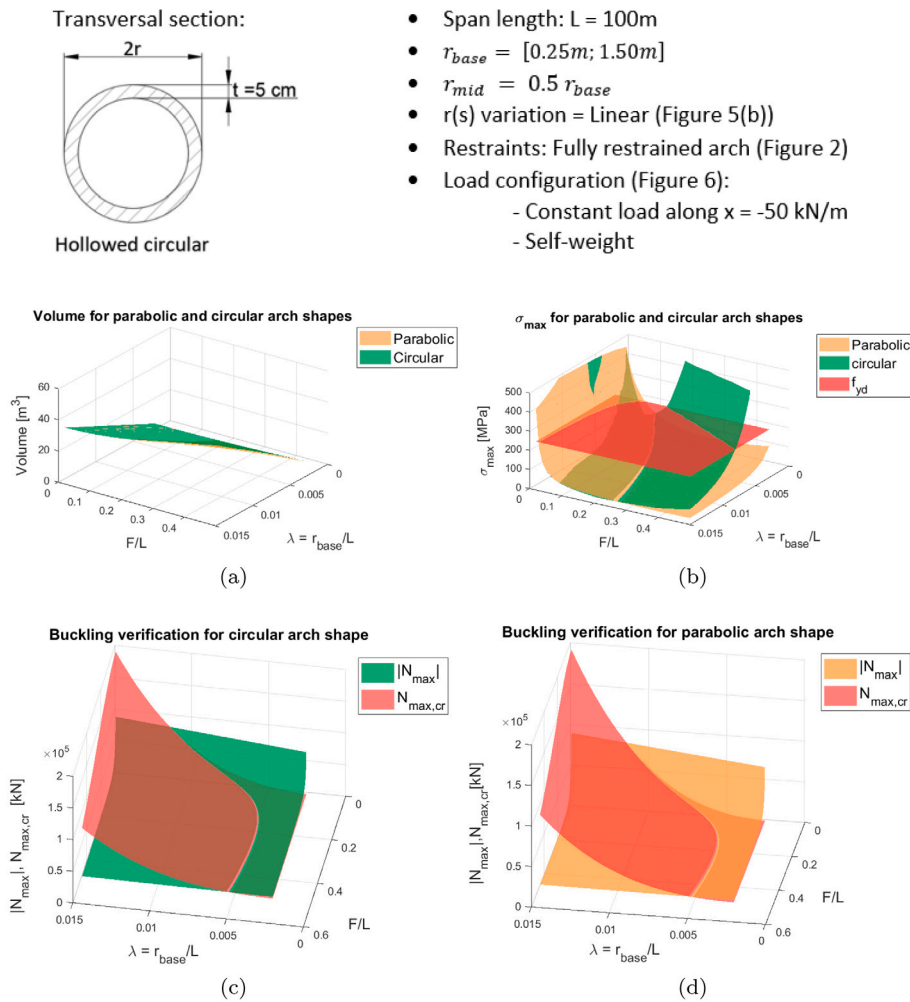


Fig. 10. Parabolic and circular arch configuration with hollow circular cross-section. Volume as function of  $F/L$  and  $r_{base}/L$  (a), Maximum Von Mises stress acting as function of  $F/L$  and  $r_{base}/L$  (b), Buckling verification for circular (c) and parabolic (d) arch shape.

tapering function, loading and boundary conditions are presented. Four different shapes are considered for the arch axis, i.e. parabolic, circular and two fourth-order polynomials. These comparisons can be used to draw interesting design indications regarding the design parameters that define the arch geometry. To this end, two design parameters are considered for each case study. They are the rise to span ratio  $F/L$  and the ratio between the characteristic size of the base cross section  $r_{base}$  and the arch span  $L$ . Mentioned case studies are subjected to the same conditions and their performances are compared in terms of total volume of structural material and maximum value of Von Mises stress. In addition, the maximum value of the Von Mises stress computed for each case study is compared with the material strength in order to define an admissibility domain for the design parameters  $F/L$  and  $r_{base}/L$ . Notice that in the presented examples the safety factors relevant to load and material strength values are not considered.

Finally, considering that the problem of structural buckling, in some cases, may be more stringent than the purely tensional problem, we considered global buckling of arches by implementing the simplified method proposed by Attard et al. (2014). As stated by the authors, although approximated, their estimate of the critical axial force is safe. More refined formulations for global buckling can be included in proposed formulation as well as an extension of the method to include nonlinear material response, see, e.g., Melchiorre et al. (2022).

#### 4.2.1. Arches loaded by vertical loads uniformly distributed along their horizontal projection

The first set of analyses regards to arches having a circular hollow cross section subjected to the self-weight and to a vertical load uniformly distributed along  $x$ . Fig. 10(a) shows that for all considered values of the rise to span ratio  $F/L$  and section characteristic size  $r_{base}$ , the volumes associated to either the circular and parabolic arches are very similar. On the contrary, a similar comparison made for arches defined by a fourth order polynomial have a volume that significantly depends on the value of the slope  $S$  at springers. This is shown in Fig. 11(a), where the volumes computed for arches generated by assuming  $S = 3.5F/L$  and  $S = 5F/L$  are compared.

Figs. 10(b) and 11(b) the same set of arches are compared in terms of maximum values of Von Mises stress. In these figures we also report the limit value  $f_y$  representing the yield stress associated to steel S355.

Finally, as far as buckling verifications are concerned, in the graphs (c) and (d) in Figs. 10 and 11, the comparisons in terms of maximum acting axial force and critical axial force computed by mentioned simplified method are shown for each studied arch shape. In these graphs, the red surface represents the critical limit axial force due to buckling  $N_{max,cr}$ , while the other surfaces represent the maximum absolute value of the axial force calculated for each arch configuration  $|N_{max}|$ .

For a greater clarity of reading, the three-dimensional graphs in Figs. 10 and 11 have been projected in two dimensions going to constitute, for each geometry of the axis of the arch, a different graph

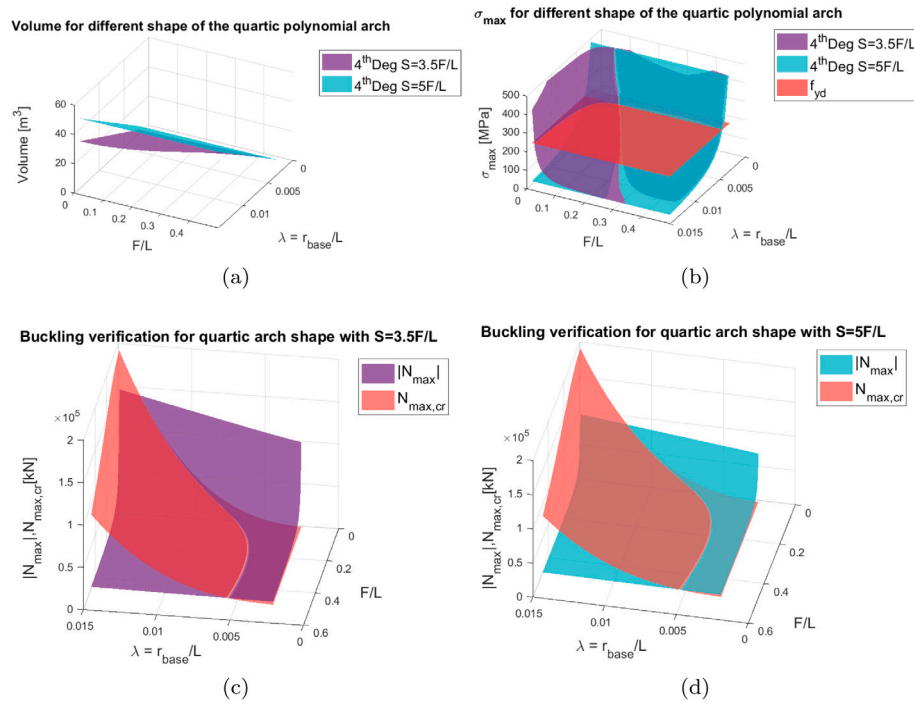


Fig. 11. Quartic polynomial shape arch configuration with hollowed circular cross-section. Volume as function of  $F/L$  and  $r_{base}/L$  (a), Maximum Von Mises stress acting as function of  $F/L$  and  $r_{base}/L$  (b), Buckling verification for quartic arch shape with  $S = 3.5F/L$  (c) and  $S = 5F/L$  (d).

in which it is possible to clearly identify the geometric configurations able to support the applied loads. In fact, in Fig. 12, the area in red represents the domain of the unfeasible configurations, while the one in white encloses all the feasible configurations within the search space. Finally, in the graphs the objective function is represented by means of contour lines and the lowest volume configuration is identified by the point in red. These graphs can be seen as abacuses that allow the designer, not only to immediately identify the feasible geometric configuration with less volume, but also to evaluate the volume variations that would be obtained by deciding to adopt different geometric configurations. In other words, the designer can choose to vary the parameters of the radius of the transverse section and the degree of arch lowering, according to what he considers most appropriate, while having control of the volumetric variations of the different configurations and of which geometries are able to support the applied loads.

In particular, Figs. 12(a) and 12(b) show that the parabolic arch performs better than the circular since in the case of circular shape, under a constant load along the  $x$ -axis, the unfeasible domain is slightly bigger. It is also possible to note that, in the research domain considered, the minimum volume configuration is very similar for both geometries. The difference is instead evident in the case of very high arches.

In the case of fourth-order polynomial arc shapes, looking at the Figs. 12(c) and 12(d) it is possible to notice that the configuration with  $S = 5.0F/L$  performs slightly better when  $F/L$  is small, while for higher  $F/L$  both geometries exhibit similar performances for all characteristic size of the cross section  $r_{base}$ .

#### 4.2.2. Arches loaded along the radial direction

A similar parametric study is performed on arches having a hollow square cross section of uniform thickness  $t = 100$  mm, whose characteristic size  $r_{base}$  is kept constant along the arch. This set of arches are subjected to distributed loads applied along the radial direction and to the arch's self-weight. Fig. 13 report the computed arch volume for all the four considered shapes and the feasible domain considering the maximum Von Mises stress applied on the studied arch configurations.

It can be seen from the graphs in Fig. 13 that, in this case, since the load is applied radially, the arc shape characterized by a larger feasible

domain is that of circular arc shape. This is an expected result and a further validation of the feasibility of the proposed method.

#### 4.2.3. Arches loaded on the mid-third of their length

The third case study regards arches with hollow rectangular cross sections having the characteristic size  $r_1$  quadratically varying between the springers and the mid-span. This set of arches are loaded by their self weight and by a uniform load applied at its mid-third, see, e.g., the last loading condition in Fig. 6. Notice that the length of the loaded region varies as a function of the total length of the arch and hence as a function of its rise  $F$ . For this reason, this particular case study is particularly significant to verify the versatility of proposed approach.

Figs. 14(a) and 14 show that this set of arches behave similarly to the case of Section 4.2.1. In particular, parabolic arches perform better than circular ones in reducing the unfeasible area, due to the tensional and buckling verifications, and this also allow to reduce the total volume of employed materials. The best performance is given by quartic arch with  $S = 3.5F/L$ , while the worst is given by the quartic shape with  $S = 5F/L$ . This may be due to the fact that the shape of arcs with low  $S$  have a parabolic-like shape while arcs with high  $S$  are more like circular arches.

#### 4.2.4. Arches loaded over one half their length

The final case study refers to an arch having a solid circular cross section whose radius varies along the arch's axis. Notice that solid circular steel sections are generally avoided in practical applications and this case study is merely academic. Actually, it has the scope of further validating the presented approach by showing how it can be used to model non symmetric loading conditions. Also, it will be shown how the presented parametric analysis can be used to highlight the better performances of hollowed sections with respect to solid ones.

The considered arch is loaded by it self-weight and by a vertical load uniformly distributed over one half of its length. These plots are qualitatively similar to the corresponding diagrams reported for previous case studies. However, a great difference is shown in quantitative terms: the employment of a solid cross section obviously implies a total volume

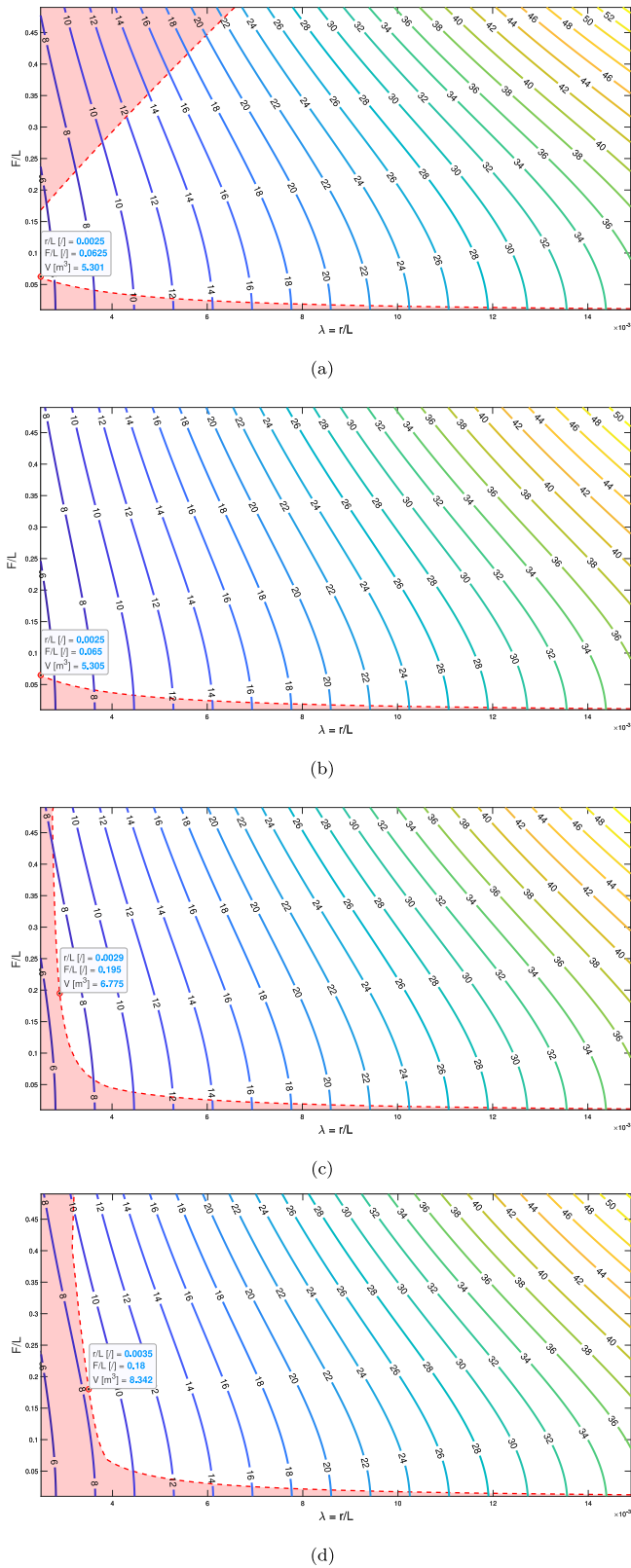


Fig. 12. Summary graphs with volumes and feasible domain for arch configurations described in Section 4.2.1: Circular shape (a), Parabolic shape (b), Quartic polynomial shape with  $S = 3.5F/L$  (c), Quartic polynomial shape with  $S = 5F/L$  (d).

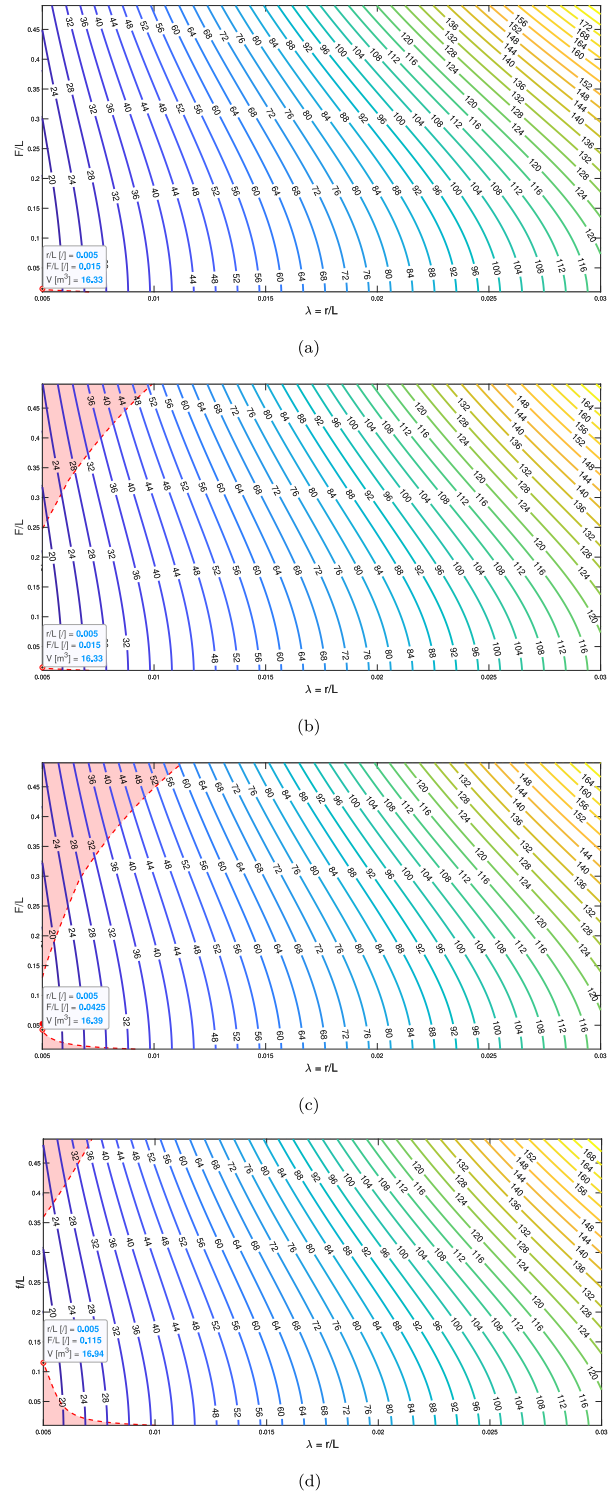
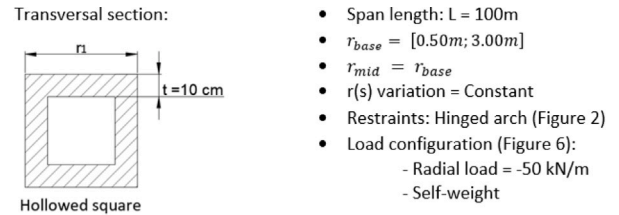
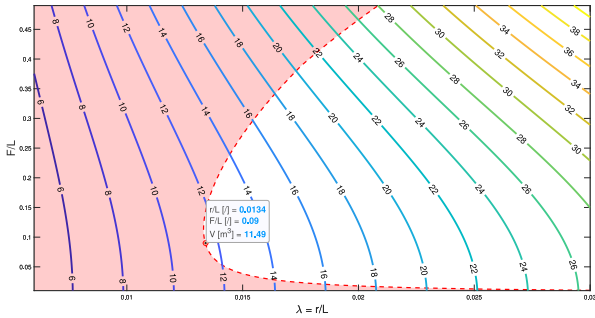
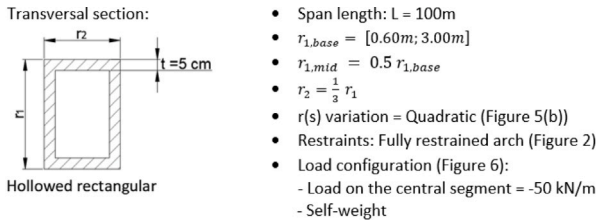
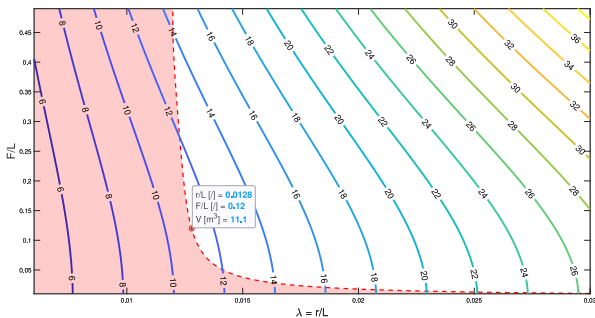


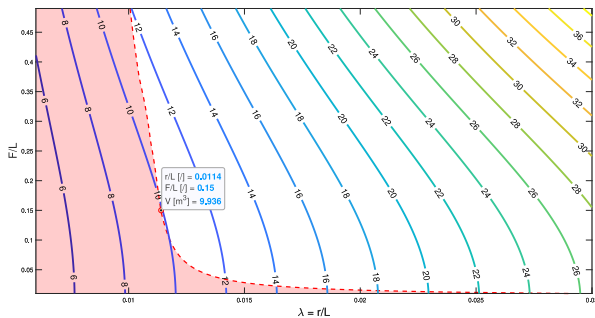
Fig. 13. Summary graphs with volumes and feasible domain for arch configurations described in Section 4.2.2: Circular shape (a), Parabolic shape (b), Quartic polynomial shape with  $S = 3.5F/L$  (c), Quartic polynomial shape with  $S = 5F/L$  (d).



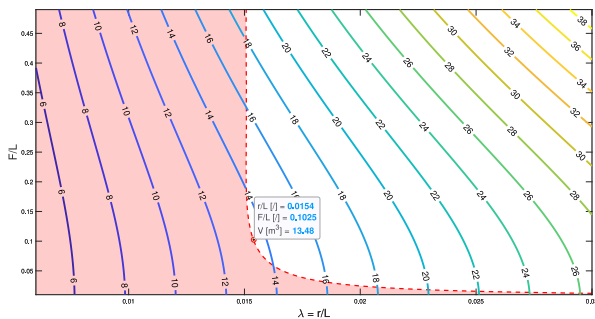
(a)



(b)

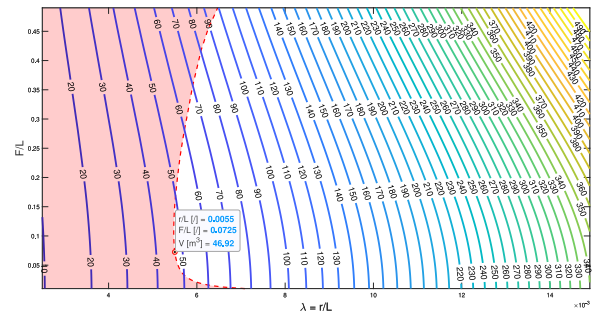
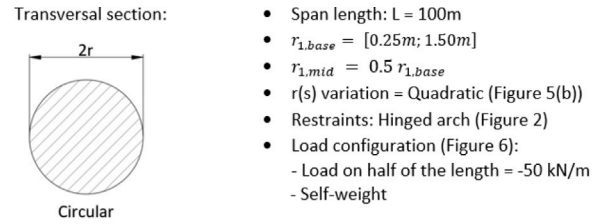


(c)

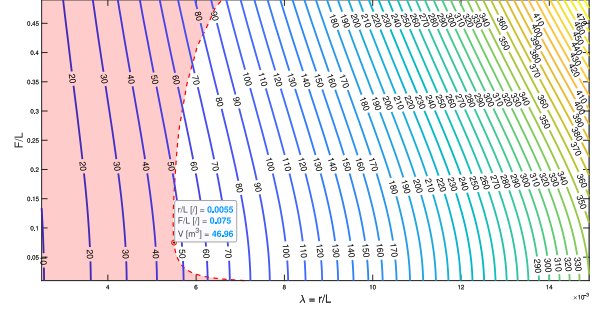


(d)

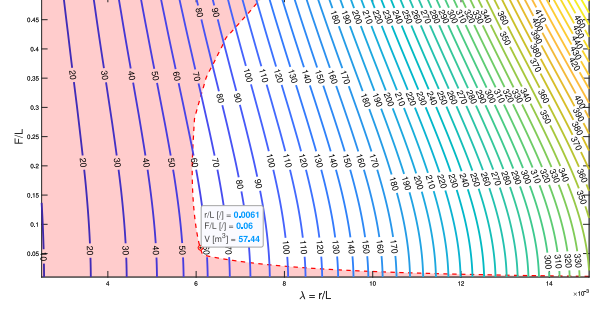
Fig. 14. Summary graphs with volumes and feasible domain for arch configurations described in Section 4.2.1: Circular shape (a), Parabolic shape (b), Quartic polynomial shape with  $S = 3.5F/L$  (c), Quartic polynomial shape with  $S = 5F/L$  (d).



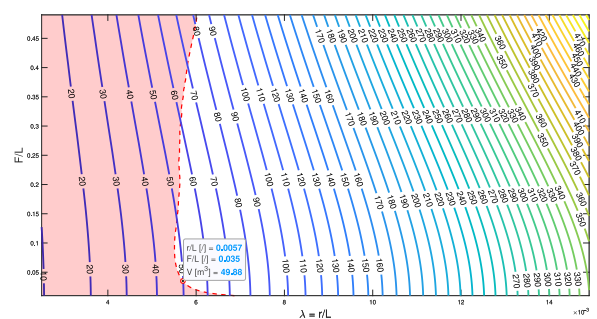
(a)



(b)



(c)



(d)

Fig. 15. Summary graphs with volumes and feasible domain for arch configurations described in Section 4.2.1: Circular shape (a), Parabolic shape (b), Quartic polynomial shape with  $S = 3.5F/L$  (c), Quartic polynomial shape with  $S = 5F/L$  (d).

that is even one order of magnitude larger than the one associated with hollow cross sections.

Fig. 15(a) and 15(b) show that both the parabolic and circular arches have similar performances in terms of volumes, since the feasible domain is practically the same. Instead, for polynomial arches, the performances of shapes having higher slope at supports, i.e.  $S = 5F/L$ , perform better than those having  $S = 3.5F/L$ , see, i.e., Fig. 15(c) and 15(d).

## 5. Conclusion

An analytical formulation for the evaluation of displacements, internal forces and Cauchy stresses in arches of different shapes (circular, quadratic and quartic polynomial), different cross-section, tapering function and loading combinations is proposed. Proposed formulation employs a sixth order differential equation and proper boundary conditions to model the mechanical behavior of the arch. It is solved with respect to the main kinematic unknown  $u$ , which represents the tangential component of the displacement of the generic cross section of the arch. The numerical solution of basic equations is obtained by an ad hoc implementation of the finite difference method approach. Several numerical examples are reported in order to demonstrate the validity of our results, which are compared with finite element solutions, and to show the versatility of the presented approach to solve parametric analyses useful to derive practical indications regarding the optimal configuration of arches of variable curvature and tapered cross section. In particular, results are reported for hollow circular, hollow square, hollow rectangular and filled circular sections. These shapes are either kept constant or are tapered according to a linear or a quadratic law along the arch's axis. Different loading combinations are considered, such as vertical or radial loads uniformly applied along the arch axis or along its horizontal projection. The cases of arches loaded only cover one portion of their length are also considered. Results of the parametric analyses are used to give to the designer a tool to compare different design solutions in terms of maximum Von Mises stresses, global buckling, and structural volume. In this way the designer has the possibility to identify not only the solution with the lowest cost of material used, but also the opportunity to study and compare different configurations to define the one that best suits the specific project. The large number of cases presented in the parametric study shows how the presented solution method can be widely employed by structural engineers and researchers interested in the optimization of this kind of structures.

## Declaration of competing interest

The authors declare that they have no known competing financial interests or personal relationships that could have appeared to influence the work reported in this paper.

## Data availability

Data will be made available on request.

## References

- Aita, Danila, Barsotti, Riccardo, Bennati, Stefano, 2015. Some explicit solutions for nonlinear elastic depressed masonry arches loaded to collapse. In: XXII Congresso AIMETA. Genova, pp. 354–359.
- Alexakis, Haris, Makris, Nicos, 2015. Limit equilibrium analysis of masonry arches. *Arch. Appl. Mech.* 85 (9), 1363–1381.
- Allen, Edward, Zalewski, Waclaw, 2009. *Form and Forces: Designing Efficient, Expressive Structures*. John Wiley & Sons.
- Attard, Mario M., Zhu, Jianbei, Kellermann, David C., 2014. In-plane buckling of prismatic funicular arches with shear deformations. *Arch. Appl. Mech.* 84 (5), 693–713.
- Bauer, AM, Breitenberger, Michael, Philipp, B, Wüchner, Roland, Bletzinger, K-U, 2016. Nonlinear isogeometric spatial Bernoulli beam. *Comput. Methods Appl. Mech. Engrg.* 303, 101–127.
- Benedetti, Andrea, Tralli, Antonio, 1989. A new hybrid FE model for arbitrarily curved beam—I. Linear analysis. *Comput. Struct.* 33 (6), 1437–1449.
- Bertetto, A, Manuello, Marano, G.C., 2022. Numerical and dimensionless analytical solutions for circular arch optimization. *Eng. Struct.* 253, 113360.
- Bresse, M., 1854. *Recherches Analytiques sur la Flexion et la Résistance des Pièces Courbes*. Mallet-Bachelier; Carilian-Goeury et Vt. Dalmont.
- Bruno, D., Lonetti, P., Pascuzzo, A., 2016. An optimization model for the design of network arch bridges. *Comput. Struct.* 170, 13–25.
- Carpinteri, Alberto, 2013. *Structural Mechanics Fundamentals*. CRC Press.
- El Zareef, Mohamed A., El Madawy, Mohamed E., Ghannam, Mohamed, 2019. Developed mathematical model for indeterminate elements with variable inertia and curved elements with constant cross-section. *Adv. Civ. Eng.* 2019.
- Eliáš, Jan, Miča, Lumír, et al., 2013. Shape optimization of concrete buried arches. *Eng. Struct.* 48, 716–726.
- Farshad, Mehdi, 1976. On optimal form of arches. *J. Franklin Inst. B* 302 (2), 187–194.
- Glisic, Branko, 2019. Simplified closed-form expressions for horizontal reactions in linear elastic arches under self-weight. In: *Proceedings of IASS Annual Symposia, 2019*. International Association for Shell and Spatial Structures (IASS), pp. 1–8.
- Gray, Alfred, Abbena, Elsa, Salamon, Simon, 2017. *Modern Differential Geometry of Curves and Surfaces with Mathematica®*. Chapman and Hall/CRC.
- Habbal, A., 1998. Direct approach to the minimization of the maximal stress over an arch structure. *J. Optim. Theory Appl.* 97 (3), 551–578.
- Halpern, Allison B., Adriaenssens, Sigrid, 2015a. In-plane optimization of truss arch footbridges using stability and serviceability objective functions. *Struct. Multidiscip. Optim.* 51 (4), 971–985.
- Halpern, Allison B., Adriaenssens, Sigrid, 2015b. In-plane optimization of truss arch footbridges using stability and serviceability objective functions. *Struct. Multidiscip. Optim.* 51 (4), 971–985.
- Heyman, Jacques, 1969. The safety of masonry arches. *Int. J. Mech. Sci.* (ISSN: 0020-7403) 11 (4), 363–385. [http://dx.doi.org/10.1016/0020-7403\(69\)90070-8](http://dx.doi.org/10.1016/0020-7403(69)90070-8), URL <https://www.sciencedirect.com/science/article/pii/0020740369900708>.
- Heyman, Jacques, Jacques, Heyman, 1998. *Structural Analysis: A Historical Approach*. Cambridge University Press.
- Hu, Chang-Fu, Pi, Yong-Lin, Gao, Wei, Li, Li, 2018. In-plane non-linear elastic stability of parabolic arches with different rise-to-span ratios. *Thin-Walled Struct.* 129, 74–84.
- Hu, Changfu, Wan, Yi, ShangGuan, Xing, 2010. A new practice in the design of arch axis. In: *Proceedings of the Th International Conference on Arch Bridges*. pp. 709–715.
- Ibrahimbegović, Adnan, 1995. On finite element implementation of geometrically nonlinear Reissner's beam theory: three-dimensional curved beam elements. *Comput. Methods Appl. Mech. Engrg.* 122 (1–2), 11–26.
- Jasińska, Dorota, Kropiowska, Dorota, 2018. The optimal design of an arch girder of variable curvature and stiffness by means of control theory. *Math. Probl. Eng.* 2018.
- Jirásek, Milan, La Malfa Ribolla, Emma, Horák, Martin, 2021. Efficient finite difference formulation of a geometrically nonlinear beam element. *Internat. J. Numer. Methods Engrg.* 122 (23), 7013–7053.
- Kimura, Toshiaki, Ohsaki, Makoto, Fujita, Shinnosuke, Michiels, Tim, Adriaenssens, Sigrid, 2020. Shape optimization of no-tension arches subjected to in-plane loading. *Structures* 28, 158–169.
- Kumarci, K., Dehkordy, P.K., Mahmodi, I., et al., 2009. Optimum shape in brick masonry arches under dynamic loads by cellular automata. *J. Civ. Eng.* 37 (1), 73–90.
- Kurrer, Karl-Eugen, 2008. The history of the theory of structures: from arch analysis to computational mechanics. *Int. J. Space Struct.* 23 (3), 193–197.
- Lewis, W.J., 2016. Mathematical model of a moment-less arch. *Proc. R. Soc. Lond. Ser. A Math. Phys. Eng. Sci.* 472 (2190), 20160019.
- Li, Yong, Huang, Surong, Lin, Chun, Gu, Quan, Qiu, Zhijian, 2017. Response sensitivity analysis for plastic plane problems based on direct differentiation method. *Comput. Struct.* 182, 392–403.
- Litewka, Przemyslaw, Rakowski, Jerzy, 1997. An efficient curved beam finite element. *Internat. J. Numer. Methods Engrg.* 40 (14), 2629–2652.
- Manuello, Amedeo, 2020. Multi-body rope approach for grid shells: Form-finding and imperfection sensitivity. *Eng. Struct.* 221, 111029.
- Marano, Giuseppe Carlo, Trentadue, Francesco, Petrone, Floriana, 2014. Optimal arch shape solution under static vertical loads. *Acta Mech.* 225 (3), 679–686.
- Marmo, Francesco, 2021. ArchLab: a MATLAB tool for the thrust line analysis of masonry arches. *Curved Layer. Struct.* 8 (1), 26–35.
- MATLAB, 2019. version (R2019b). The MathWorks Inc., Natick, Massachusetts, URL <https://www.mathworks.com/products/matlab.html>.
- McCullough, Conde Balcom, Thayer, Edward S., 1931. *Elastic Arch Bridges*. J. Wiley & Sons, Incorporated.
- Melchiorre, Jonathan, Bertetto, Amedeo Manuello, Marano, Giuseppe Carlo, 2021. Application of a machine learning algorithm for the structural optimization of circular arches with different cross-sections. *J. Appl. Math. Phys.* 9 (5), 1159–1170.
- Melchiorre, Jonathan, Manuello, Amedeo, Sardone, Laura, Marano, Giuseppe Carlo, 2022. Damaging configurations in arch structures with variable curvature and tapered cross-section. In: *Proceedings of the 15th World Congress on Computational Mechanics*.

- Michiels, Tim, Adriaenssens, Sigrid, 2018. Form-finding algorithm for masonry arches subjected to in-plane earthquake loading. *Comput. Struct.* 195, 85–98.
- MidasGEN, 0000. URL <https://www.midasoft.com/building/products/midasgen>.
- Nascimbene, R., 2013. An arbitrary cross section, locking free shear-flexible curved beam finite element. *Int. J. Comput. Methods Eng. Sci. Mech.* 14 (2), 90–103.
- Ochsendorf, John, 2006. Masonry arch on spreading supports. *Struct. Eng.* 84 (2), 29–34.
- Osserman, Robert, 2010. How the gateway arch got its shape. In: *Recalling Eero Saarinen 1910–2010*. Springer, pp. 167–189.
- Park, Jaegyun, Chun, Yun-Hee, Lee, Jungwhae, 2016. Optimal design of an arch bridge with high performance steel for bridges using genetic algorithm. *Int. J. Steel Struct.* 16 (2), 559–572.
- Pi, Y.-L., Bradford, M.A., Tin-Loi, F., Gilbert, R.I., 2007. Geometric and material nonlinear analyses of elastically restrained arches. *Eng. Struct.* 29 (3), 283–295.
- Pouraminian, Majid, Ghaemian, Mohsen, 2015. Shape optimisation of concrete open spandrel arch bridges. *Grđevinar* 67 (12.), 1177–1185.
- Shi, Can, Zhao, Chunfa, Zhang, Xu, Andersson, Andreas, 2020. Analysis on dynamic performance of different track transition forms using the discrete element/finite difference hybrid method. *Comput. Struct.* 230, 106187.
- Sonavane, Trupti, 2014. *Analysis of Arches* (Ph.D. thesis). University of Colorado at Boulder.
- Szefer, G., Mikulski, L., 1984. Optimal design of elastic arches with I cross-section. *Eng. Trans.* 32 (4), 467–480.
- Trentadue, Francesco, Marano, Giuseppe Carlo, Vanzi, Ivo, Briseghella, Bruno, 2018. Optimal arches shape for single-point-supported deck bridges. *Acta Mech.* 229 (5), 2291–2297.
- Tufekci, Ekrem, Eroglu, Ugurcan, Aya, Serhan Aydin, 2017. A new two-noded curved beam finite element formulation based on exact solution. *Eng. Comput.* 33 (2), 261–273.
- Wang, C.Y., Wang, CM3323269, 2015. Closed-form solutions for funicular cables and arches. *Acta Mech.* 226 (5), 1641.
- Winkler, Emil, 1858. Formänderung und Festigkeit gekrümmter Körper, insbesondere der Ringe. *Civilingenieur* 4, 232–246.